J Solid State Electrochem (2011) 15:1193–1199
DOI 10.1007/s10008-010-1181-y

ORIGINAL PAPER

Electrochemical preparation and magnetic properties of submicron Co_xPb_{1-x} dendrites

Chen-Zhong Yao · Hui-Xuan Ma · Xi-Sheng Zhang · Li-Xin Meng · Li-Ping Zhao · Ling Tai · Yu-Chun Wang · Qiao-Juan Gong · Ye-Xiang Tong

Received: 25 April 2010 / Revised: 5 August 2010 / Accepted: 6 August 2010 / Published online: 16 September 2010

Abstract Magnetic dendrites of Co_xPb_{1-x} were fabricated through potentiostatic electrochemical deposition on Cu substrates in boric acid solution at room temperature. The as-deposited dendrites were determined by scanning electron microscopy (SEM), X-ray diffraction (XRD), transmission electron microscopy (TEM), electrodeposition (ED), and energy dispersive X-ray spectroscopy (EDS). SEM results indicate that the Co_xPb_{1-x} dendrites are highly symmetrical in structures. The diameters of the branches are about 50~200 nm, and the backbones are continuous with lengths up to about 10 μm. XRD patterns show that the as-deposited dendrites are solid solutions. The annealing treatment can result in the recrystallization of these metastable alloys into two separate phases. TEM, ED, and EDS results also reveal that the backbones and the branches of the dendrites are composed of different amounts of cobalt. Magnetic measurements confirm that the as-deposited Co_xPb_{1-x} dendrites have a softly ferromagnetic behavior, and a small coercive force (about 80 Oe). Also the saturation magnetizations of the Co_xPb_{1-x} dendrites decrease rapidly with the temperature increasing.

C.-Z. Yao · H.-X. Ma · X.-S. Zhang · L.-X. Meng · L.-P. Zhao · L. Tai · Y.-C. Wang · Q.-J. Gong
Yuncheng University,
Yuncheng 044000, People's Republic of China

C.-Z. Yao (✉) · Y.-X. Tong
Ministry of Education Key Laboratory of Bioinorganic and Synthetic Chemistry, School of Chemistry and Chemical Engineering, Institute of Optoelectronic and Functional Composite Materials, Sun Yat-Sen University,
Guangzhou 510275, People's Republic of China
e-mail: yaochzh1999@126.com

Keywords Electrodeposition · Dendrites · Electron diffraction · Magnetic properties

Introduction

Synthesis of metal alloy with controlled size, morphology, and crystal orientation has been a booming research field in the last decades because of their unique physical and chemical properties different from bulk alloys. The introduction of magnetic elements into nonmagnetic matrix has an important effect on the morphologies, structures, and magnetic properties of the alloy for ferromagnetic-nonmagnetic alloy. Comparing to physical methods such as vapor deposition and molecular beam epitaxy, electrochemical deposition (ECD) of metal alloy has significantly advantages in the production of alloy because it does not require expensive instrumentations, high temperatures, and low-vacuum pressures [1]. Additionally, different patterns such as stringy, dendrite, open ramified, and dense branching morphology, are reported for copper, zinc, and other metals prepared by ECD [2–16]. The shaping of these structures can be achieved by well-controlled ECD parameters such as depositing voltage, plating concentration, and cell thickness. Among these reports, much attention has been paid to the shaping mechanisms of these morphologies, including the transport mechanism, interface kinetics, crystallographic orientation, and chemical compositions of the electrolyte.

Pb alloys have received considerable attention for many decades because of their wide applications as semiconductors [17–19], thermoelectric materials [20–23], ferroelectrics [24–27], catalysts [28, 29], magnetic materials [30–32], and heat-carriers for nuclear reactors [33]. Nunes et al. [34] studied the solubility limit of metastable Pb/Fe

alloys in the Fe and Pb sides of the composition range, by combining the vapor quenching and high-energy milling techniques. Touboltsev et al. [35] prepared metastable Pb–Ni alloy through high-fluence ion implantation, and recently Ji et al. [32, 36] fabricated Pb–Co, Pb–Ni nanowire arrays by ECD in porous AAO and showed the variation of coercivities as a function of annealing temperature.

Although many studies have provided the fascinating morphologies of metal alloy, there have been few reports on M–Pb (M=Fe, Co, Ni) binary magnetic alloys by ECD method without templates. In this paper, we demonstrate one-step and template-free ECD for the large-scale fabrication of submicron Co_xPb_{1-x} dendrites on Cu substrates. The morphology of submicron Co_xPb_{1-x} dendrites can be readily tuned by adjusting the deposition conditions. Moreover, the effects of the annealing treatment on the structures and magnetic properties of these submicron dendrites are also studied.

Experimental

Reagents

All the reagents of analytical grade were purchased from Guangdong Guanghua Chemical Reagents Factory and used directly without any purification. Deionized water was used throughout the experiments.

Preparation of Co_xPb_{1-x} dendrites

A simple three-electrode cell was used in our experiments. The anode and cathode were separated by porous wall. The experiments were carried out at room temperature by using a homemade potentiostatic apparatus. A pure Cu wire (99.99%, 0.085 cm^2) was used as working electrode in the process of cyclic voltammetric tests, and a pure Cu plate (99.99%, 1.0 cm^2) was used as working electrode during the ECD. The Cu electrode was polished by SiC abrasive paper from 300 to 800 grits. After dipped in HCl (5%) for 10 min, it was washed by distilled water, and rinsed with acetone in ultrasonic bath before each experiment. A graphite electrode was used as a counter electrode (spectral grade, 1.8 cm^2). A saturated calomel electrode (SCE) was used as the reference electrode which was connected to the cell with a double salt bridge system. All the potential values determined in this study refer to the SCE. ECD of Co_xPb_{1-x} dendrites was performed in solution of 0.03 M $CoCl_2$ + 0.01 M $Pb(NO_3)_2$ + 0.2 M NH_4Cl + 0.5 M H_3BO_3 with a pH value of 5.68. The boric acid was added into the solution as a buffer to avoid the local pH rise caused by parallel hydrogen evolution reaction [37, 38]. When the reaction was finished, the deposited films were removed from the electrolyte and rinsed with distilled water and acetone.

Annealing treatment of Co_xPb_{1-x} dendrites

The as-deposited Co_xPb_{1-x} dendrites, prepared in the working bath by applying −1.0 V for 1 min, were heated from 303 K to the setting temperatures (573, 600, 623, and 673 K) at a heating rate of 10 K/min in a quartz tube under N_2 atmosphere and then held at each temperature for 20 min. The tube was removed from the furnace and allowed to cool to room temperature.

Analysis

A CHI 750B electrochemical workstation was used for the electrochemical measurements. The ECD experiments were carried out at room temperature by using a homemade potentiostatic apparatus. Energy dispersive X-ray spectroscopy (EDS, Oxford-INCA) and X-ray diffraction (XRD, Rigaku, D/MAX 2200 VPC) were used to determine the deposits composition and structure, respectively. Thermal field emission scanning electron microscopy (TFE-SEM, FEI, Quanta 400) and transmission electron microscope (TEM, JEM-2010HR) were used to investigate the surface morphologies of the films. Superconducting quantum interference device (SQUID, Quantum Design, MPMS XL-7) measurements were carried out to investigate the magnetic behaviors of the Co_xPb_{1-x} dendrites at room temperature.

Results and discussions

Electrochemical measurements

The cyclic voltammetric (CV) measurements of Cu electrode were used to define the potential range. Figure 1a shows CV curve in solution of 0.01 M $Pb(NO_3)_2$ + 0.2 M NH_4Cl + 0.5 M HBO_3. The reduction wave of Pb^{2+} to Pb is about −0.58 V and the oxidation wave is −0.37 V. The reduction wave at about −0.89 V corresponds to the reduction of Co^{2+} to Co, and the oxidation wave at about −0.39 V is the anodic stripping of Co as shown in Fig. 1b. Figure 1c shows the CV curves in different potential scanning ranges in solution of 0.03 M $CoCl_2$ + 0.01 M $Pb(NO_3)_2$ + 0.2 M NH_4Cl + 0.5 M HBO_3. Compared with Fig. 1a, similar reduction and oxidation peaks in the range of −0.8~0 V are observed in Fig. 1c. For the CV curves in the wider ranges (−1.0~0 V and −1.3~0 V), two reduction waves are observed respectively. The wave (I) corresponds to the reduction of Pb^{2+} to Pb, and the wave (II) corresponds to the reduction of Co^{2+} to Co. The oxidation peaks labeled as (III) at about −0.36 V are originated from

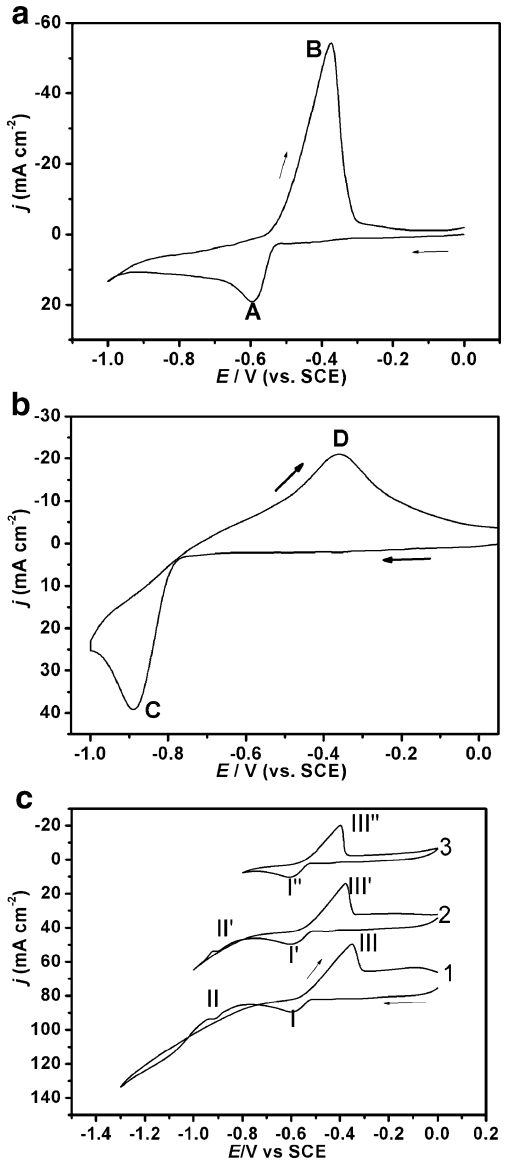

Fig. 1 Cyclic voltammograms of Cu (0.085 cm^2) electrode in solution of **a** 0.01 M $Pb(NO_3)_2$+0.2 M NH_4Cl+0.5 M HBO_3; **b** 0.03 M $CoCl_2$+ 0.2 M NH_4Cl+0.5 M H_3BO_3; **c** 0.03 M $CoCl_2$+0.01 M $Pb(NO_3)_2$+ 0.2 M NH_4Cl+0.5 M H_3BO_3 in different potential scanning ranges: (*1*) −1.3~0 V; (*2*) −1.0~0 V; and (*3*) −0.8~0 V. Scan rate, 0.1 Vs^{-1}

the stripping of Co_xPb_{1-x} deposit. Furthermore, it can be observed that the oxidation peak potential shifts to a positive value and the peak current increases as the potential scanning range becomes wider. This may be attributed to the fact that the more Co_xPb_{1-x} are deposited on the surface of Cu electrode as the cathodic potential limit shifted to a more negative direction, which makes it more difficult to dissolve into the solution [39, 40].

Characterization of Co_xPb_{1-x} dendrites

Firstly, the synthesis of Co_xPb_{1-x} deposits was performed in solution of 0.01 M $CoCl_2$ + 0.01 M $Pb(NO_3)_2$ + 0.2 M NH_4Cl + 0.5 M H_3BO_3. However, EDS result shows that the deposits only consist of pure Pb when the deposition potential is between −0.9 V and −1.3 V. Co_xPb_{1-x} dendrites were obtained at −1.0 V when the concentration of $CoCl_2$ increased to 0.03 M. It can be seen from Fig. 2a that large area of disordered dendrites is formed on the Cu substrates. Moreover, the growth direction is apparently random. EDS pattern (Fig. 2b) confirms the present of lead (75.3 at.%) and cobalt (24.7 at.%) in the deposits.

Figure 3 shows the high-resolution SEM images of the dendritic Co_xPb_{1-x} deposits obtained at −1.0 V for different time at room temperature. The backbones with short branches were obtained when the deposition time is about 30 s, as illustrated in Fig. 3a. The typical diameter of the branches is about 50~200 nm. When the ECD time increased to 1 min, the SEM observations in Fig. 3b reveal that the samples are composed of a large quantity of submicron dendrites and all the branches are grown on the roots of the burls. Namely, the dendritic backbones of Co_xPb_{1-x} deposits are formed in the beginning of the growth process, and the branches are formed in the subsequent growth process. Taking a careful observe, the surface of the dendrites is made up of lamellar Co_xPb_{1-x} deposits.

The morphology of Co_xPb_{1-x} dendrites could be further tuned by the deposition potential. The regular ramified Co_xPb_{1-x} deposits with short branches were formed when

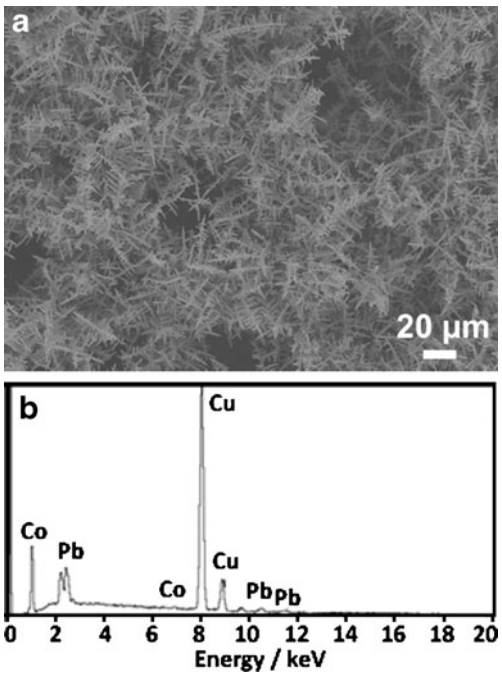

Fig. 2 **a** A typical SEM image and **b** EDS spectrum of Co_xPb_{1-x} dendrites obtained by potentiostatic electrolysis at −1.0 V in 0.03 M $CoCl_2$ + 0.01 M $Pb(NO_3)_2$ + 0.2 M NH_4Cl + 0.5 M H_3BO_3 for 1 min

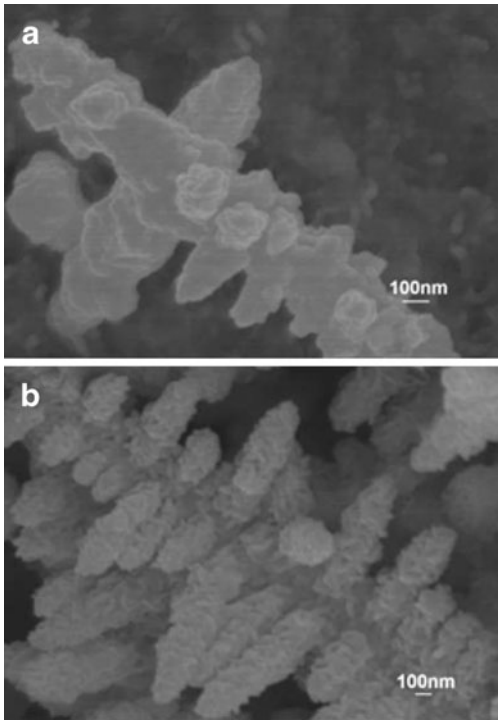

Fig. 3 High-resolution SEM images of the as-deposited Co_xPb_{1-x} dendrites prepared by potentiostatic electrolysis at −1.0 V for different time: **a** 30 s and **b** 1 min

the deposition potential increased to −1.3 V. The typical SEM images of these dendrites are shown in Fig. 4a and b, respectively. There are four branches at nearly right angle sharply around the bough. The branches are parallel to each other in the same direction and small secondary branches emerge from these branches. The distance between the neighboring branches is about 500 nm. The component of these dendrites contains 48.1 at.% lead and 51.9 at.% cobalt, as demonstrated in Fig. 4c.

The structural details of the submicron dendrites prepared at −1.0 V were further analyzed by TEM and select area electron diffraction (SAED). Figure 5a is a low-magnification TEM image of the sample deposited for 30 s, indicating that the dendrites have a rotational C_4 symmetry. The TEM image obtained at 1 min is given in Fig. 5b, further confirming that these branches are relatively uniform with diameters of 100~200 nm and distances of about 100 nm. This result is in accordance with the SEM image (Fig. 3b). The SAED measurements confirm that the structure of the backbone is polycrystalline (Fig. 5c). Diffraction halo is also observed in the SAED pattern, which might be caused by amorphous Co and Pb oxides on the surface of the backbone. The branches of the dendrites are single crystal of face-centered-cubic (*fcc*) Pb (Fig. 5d). Notably, the element of Co is only existed in the trunk, as confirmed by the EDS patterns (Fig. 5e, f).

Based on the SEM and TEM results above, the formation process of the dendrites may be ascribed to a self-assembly process in the current reaction system [41]. The whole evolution process of the Co_xPb_{1-x} dendrites can be divided into three steps. In the initial stage, Co_xPb_{1-x} nuclei are formed via electrochemical reduction on the surface of the cathode and then form the primary nano-

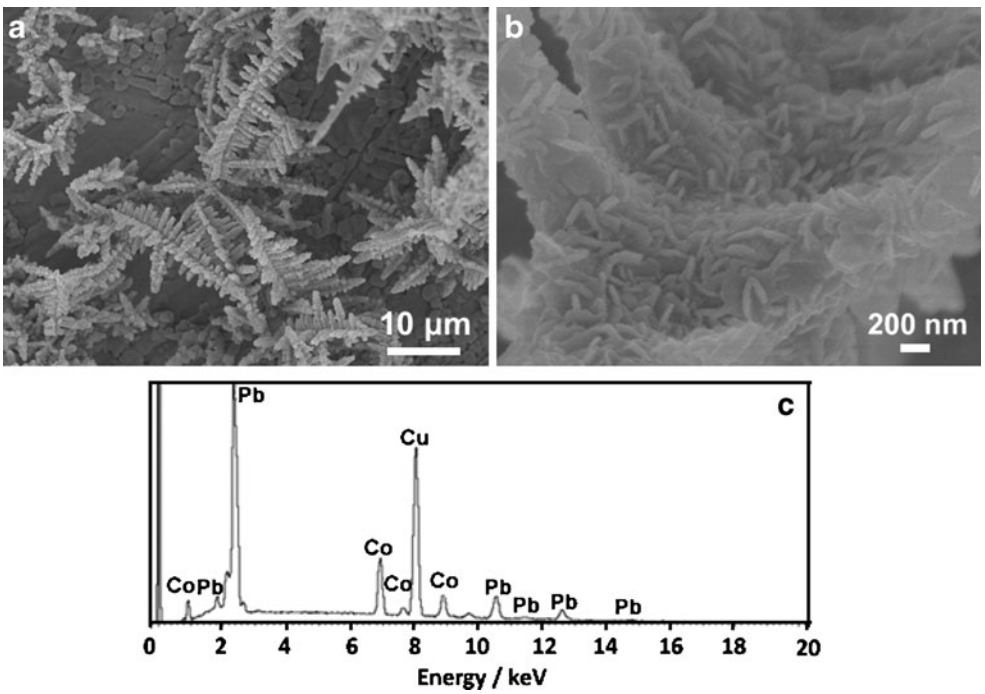

Fig. 4 **a** Typical SEM image, **b** magnified SEM image, and **c** EDS spectrum of the as-deposited Co_xPb_{1-x} dendrites obtained by potentiostatic electrolysis at −1.3 V for 1 min

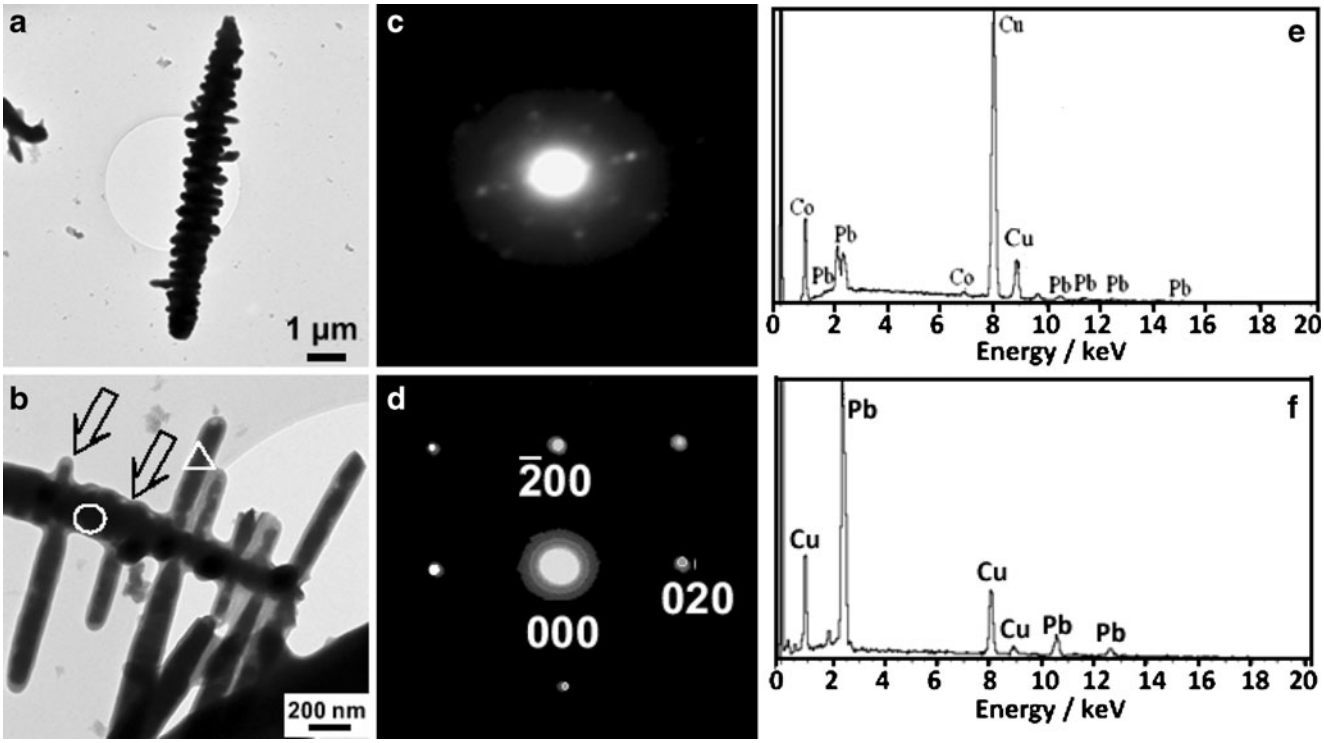

Fig. 5 TEM images of dendrites prepared at −1.0 V for different deposition time: **a** 30 s; **b** 1 min. ED and EDS patterns taken from the different areas in **b**: **c**, **e** the circle area; **d**, **f** the triangle area

particles. Secondly, these nanoparticles self-assemble to larger particles which will aggregate to large crystalline assemblages of Co_xPb_{1-x} nanorods. As known to us, building blocks mainly relies on two factors: the same or similar surface energies and the lattice matching extent of the attached surfaces. The nanoparticles have high surface energy and are metastable which can absorb new species. No matter whether the succeeding species are regular or irregular, there are always consistent junctions for them to attach because of the polycrystalline structure of the nanoparticles. The nanorods can be formed by adsorption of the diffusing Co_xPb_{1-x} nanoparticles once they are in contact with each other. The driving force for the aggregation of these nanoparticles to form nanorods and subsequently to dendrites is to reduce the surface energy from the thermodynamic viewpoint, which is similar to the formation of nanostructured Ag, Cu, Co, Ni, and Au [42–46]. Finally, with the growth and extension of the nanorods from different junctions, submicron Co_xPb_{1-x} dendritic structures are formed as shown in Fig. 5a, b.

Figure 6 shows the SEM images of the samples annealed at different temperatures. The patterns observed in these deposits were melting preliminarily, but the initial panorama of the dendritic branches could be seen at 573 K from Fig. 6a. Figure 6b and c show that the dendritic pattern almost disappeared after annealing treatment at 623 K and 673 K. Especially after annealed at 673 K, the dendrites are combined and form larger agglomerates.

The structure of Co_xPb_{1-x} dendrites

The structure of Co_xPb_{1-x} dendrites was studied by XRD using Cu K_α radiation. Figure 7 shows the XRD patterns of the as-deposited and the annealed Co_xPb_{1-x} deposits on Cu substrates. The *fcc* Pb diffraction pattern containing peaks (111) and (200) can be well identified. But the Pb diffraction peaks are shifted toward higher angles (Fig. 7a), which indicates the as-deposited dendrites in this work are solid solutions. A cobalt diffraction peak (101) (2 Theta=47.5°) corresponding to the hexagonal-close-packed (*hcp*) Co (Fig. 7d) is observed after annealed at 673 K. According to the Co–Pb binary phase diagram [47], the mutual solubility of Co and Pb is very low in both solid and liquid forms under equilibrium conditions. However, due to the high ECD rate, forming metastable solid solutions becomes possible in the as-deposited dendrites. The Co peaks appearing in the annealed sample may be attributed to the recrystallization and the phase separation of the metastable solid solution in this system. This phenomenon is similar to the Fe–Ag, Co–Cu, and Co–Ag systems [48].

Magnetic properties of Co_xPb_{1-x} dendrites

The magnetic properties of Pb alloys with magnetic elements have been scarcely studied in literature. Here we investigated the magnetic properties of the as-deposited and the annealed Co_xPb_{1-x} dendrites. Figure 8 shows the typical

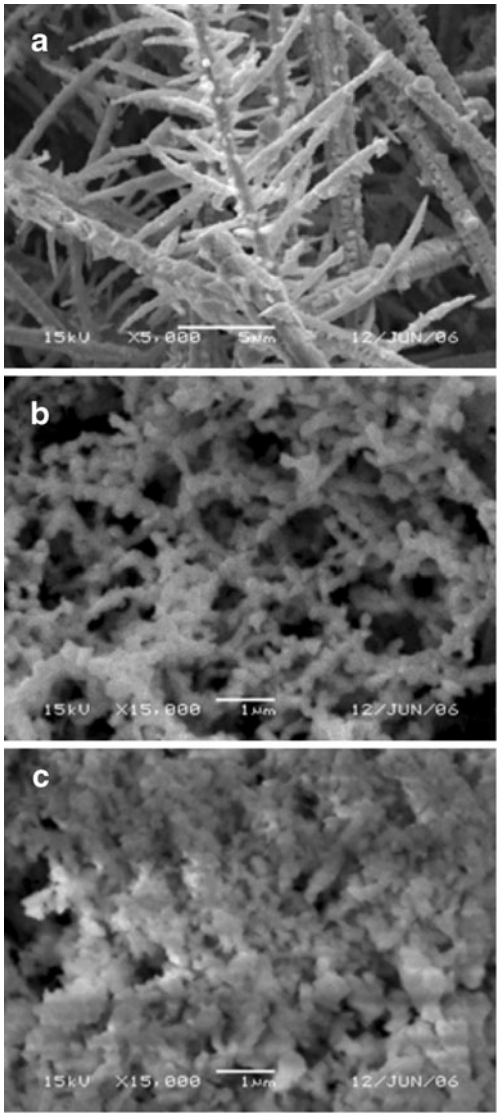

Fig. 6 SEM images of the Co_xPb_{1-x} dendrites at different annealing temperatures: **a** T=573 K; **b** T=623 K; and **c** T=673 K. The as-deposited samples were prepared at −1.0 V for 1 min

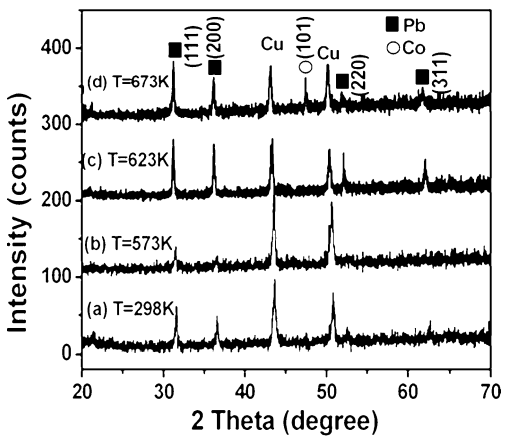

Fig. 7 XRD patterns of **a** as-deposited Co_xPb_{1-x} dendrites; annealed at different temperatures: **b** T=573 K, **c** T=623 K, and **d** T=673 K. The as-deposited samples were prepared at −1.0 V for 1 min

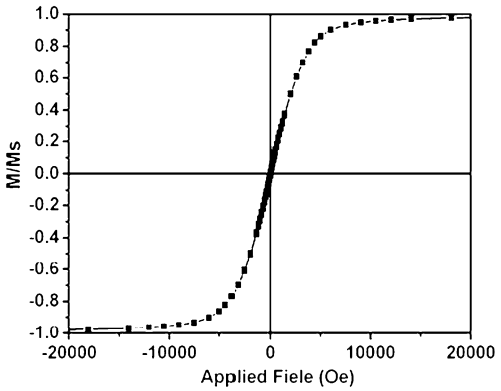

Fig. 8 Room temperature normalized magnetic hysteresis loop of the as-deposited Co_xPb_{1-x} dendrites prepared at −1.0 V for 1 min

normalized magnetic hysteresis loop of the as-deposited Co_xPb_{1-x} dendrites at room temperature in a magnetic field up to 20,000 Oe. Obviously, the samples exhibit a good softly ferromagnetic behavior, and the coercive force is about 80 Oe. The field dependence curves of magnetization (*M-H*) of the annealed dendrites at different temperatures are shown in Fig. 9. The initial susceptibility (x_i) and the saturation magnetization (M_s) decrease monotonically as the annealing treatment temperature increases. The maximum value of M_s is 0.48 emu/g for the as-deposited samples (Inset Fig. 9). Along with the annealing temperature rising, the M_s of the samples decreased continuously. The results can be explained by the following view. According to the XRD results, the element of Co is dissolved into Pb for the as-deposited samples. Along with the ECD progress, the average distribution of Co can reach a kind of well-proportioned degree approaching to single magnetic

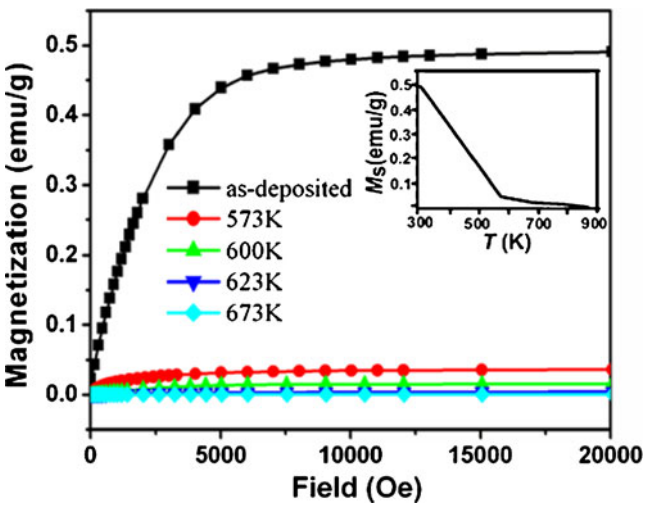

Fig. 9 The *M-H* of the as-deposited Co_xPb_{1-x} dendrites and the annealed dendrites at different temperatures measured at room temperature. The as-deposited Co_xPb_{1-x} dendrites were prepared at −1.0 V for 1 min. The *inset* shows the saturation magnetization (*Ms*) as a function of the annealing temperature for Co_xPb_{1-x} dendrites

domain in Pb as a whole. As the annealing temperature increasing, the average scattered Co accumulates gradually during the melting of Pb. The destruction and disappearance of the mixed phase and the phase separation between Co and Pb can result in the decrease of saturation magnetization.

Conclusions

Submicron dendritic Co_xPb_{1-x} magnetic deposits were successfully prepared by potentiostatic electrochemical deposition on Cu substrates. SEM and TEM observations indicate that the dendrites present rotational C_4 symmetry and the angles between the branches are right angle around the backbone axis. The Co content and the size of the dendrites increase dramatically as the deposition potential becomes more negative. The as-deposited Co_xPb_{1-x} dendrites exhibit metastable solid solutions. A phase separation into *fcc* Pb and *hcp* Co occurs in the annealed deposits. Magnetic measurements show that the coercive force of Co_xPb_{1-x} dendrites is about 80 Oe at room temperature. The saturation magnetization decreases rapidly by increasing the annealing temperature.

Acknowledgments This work was supported by Natural Science Foundation of China (no. 20873184 and 90923008), Guangdong province (no. 2008B010600040 and 9251027501000002), S & T project of Shanxi province (no. 20081044 and 200713033) and the Foundation of Yuncheng University.

References

1. Hurst SJ, Payne EK, Qin LD, Mirkin CA (2006) Angew Chem Int Ed 45:2672–2692
2. Switzer JA, Hung CJ, Huang LY, Miller FS, Zhou Y, Raub ER, Shumsky MG, Bohannan EW (1998) J Mater Res 13:909–916
3. Moran E, Cattaneo C, Mishima H, López de Mishima BA, Silvetti SP, Rodriguez JL, Pastor E (2008) J Solid State Electrochem 12:583–589
4. Fujiwara Y, Enomoto H (2004) J Solid State Electrochem 8:167–175
5. Salgado L, Meas Y, Trejo G (2002) J Solid State Electrochem 7:37–42
6. Fustes J, Gomes A, da Silva Pereira MI (2008) J Solid State Electrochem 12:1435–1443
7. Gómez E, Llorente A, Alcobe X, Vallés E (2004) J Solid State Electrochem 8:82–88
8. Bodea S, Vignon L, Ballou R, Molho P (1999) Phys Rev Lett 83:2612–2615
9. Zhang KQ, Wang M, Zhong S, Chen GX, Ming NB (2000) Phys Rev E 61:5512–5519
10. Pasquale MA, Marchiano SL, Schilardi PL, Salvarezza RC, Arvia AJ (2002) Phys Rev E 65:041608(1-5)
11. Kumar A, Biebuyck HA, Whitesides GM (1994) Langmuir 10:1498–1511
12. Kuo TC, Sloan LA, Sweedler JV, Bohn PW (2001) Langmuir 17:6298–6303
13. Lee W, Ji R, Gosele U, Nielsch K (2006) Nat Mater 5:741–747
14. Masuda H, Fukuda K (1995) Science 268:1466–1468
15. Martin CR (1994) Science 266:1961–1966
16. Xiao ZL, Han CY, Kwok WK, Wang HH, Welp U, Wang J, Crabtree GW (2004) J Am Chem Soc 126:2316–2317
17. Hu XW, Li SM, Chen WJ, Gao SF, Liu L, Fu HZ (2009) J Alloy Compd 484:631–636
18. Bouroushian M, Kosanovic T, Spyrellis N (2005) J Solid State Electrochem 9:55–60
19. Cho KS, Talapin DV, Gaschler W, Murray CB (2005) J Am Chem Soc 127:7140–7147
20. Jafarian M, Danaee I, Maleki A, Gobal F, Mahjani MG (2009) J Alloy Compd 478:83–88
21. Lu WG, Gao PX, Jian WB, Wang ZL, Fang JY (2004) J Am Chem Soc 126:14816–14821
22. Li KW, Meng XT, Liang X, Wang H, Yan H (2006) J Solid State Electrochem 10:48–53
23. Androulakis J, Hsu KF, Pcionek R, Kong H, Uher C, D'Angelo JJ, Downey A, Hogan T, Kanatzidis MG (2006) Adv Mater 18:1170–1173
24. Azuma M, Takata K, Saito T, Ishiwata S, Shimakawa Y, Takano M (2005) J Am Chem Soc 127:8889–8892
25. Sakamoto W, Masuda Y, Yogo T (2006) J Alloy Compd 408–412:543–546
26. Lu R, Hase M, Kitajima M, Nakashima S, Sugai S (2006) J Lumin 119–120:378–382
27. Hubicka Z, Cada M, Adamekc P, Virostko P, Olejnıcek J, Deynekaa A, Jastrabıka L, Jurek K, Suchaneck G, Guenther M, Gerlach G, Bohac P (2005) Surf Coat Technol 200:940–946
28. Tsud N, Dudr V, Fabík S, Brun C, Cháb V, Matolín V, Prince KC (2004) Surf Sci 560:259–268
29. Oh I, Gewirth AA, Kwak J (2003) J Catal 213:17–22
30. Peña A, Gutiérrez J, Gilde Muro I, Campo J, Barandiarán JM, Rojo T (2006) Eur J Inorg Chem 16:3227–3235
31. Gulay LD, Kaczorowski D, Shemet VY, Pietraszko A (2006) J Alloy Compd 421:87–90
32. Ji GB, Cao JM, Zhang F, Xu GY, Su HL, Tang SL, Gu BX, Du YW (2005) J Phys Chem B 109:17100–17106
33. Yagodin D, Sivkov G, Volodin S, Popel P, Mozgovoj A (2005) J Mater Sci 40:2259–2261
34. Nunes E, Passamani EC, Larica C, Freitas JCC, Takeuchi AY, Baggio-Saitovitch E, Doriguetto AC, Fernandes AAR (2005) Mater Sci Eng A 390:13–18
35. Touboltsev V, Raisanen J, Kolodyazhnaya M, Johnson E, Johansen A, Sarholt L (2002) J Appl Phys 92:895(1-7)
36. Ji GB, Tang SL, Gu BX, Du YW (2004) J Phys Chem B 108:8862–8865
37. Santos JS, Matos R, Trivinho-Strixino F, Pereira EC (2007) Electrochim Acta 53:644–649
38. Šupicová M, Rozik R, Trnková L, Oriňáková R, Gálová M (2006) J Solid State Electrochem 10:61–68
39. Baldo MA, Bragato C, Mazzocchin GA, Daniele S (1998) Electrochim Acta 43:3413–3422
40. Kirilova I, Ivanov V, Rashkov S (1998) J Appl Electrochem 28:1359–1363
41. Li GR, Zheng FL, Tong YX (2008) Cryst Growth Des 8:1226–1232
42. Maddanimath T, Kumar A, Darcy-Gall J, Ganesan P, Vijayamohanan K, Ramanath G (2005) Chem Commun 11:1435–1437
43. Yan CL, Xue DF (2008) Cryst Growth Des 8:1849–1854
44. Zhu LP, Xiao HM, Zhang WD, Yang Y, Fu SY (2008) Cryst Growth Des 8:1113–1118
45. Ye J, Chen QW, Qi HP, Tao N (2008) Cryst Growth Des 8:2464–2468
46. Qin Y, Song Y, Sun NJ, Zhao NN, Li MX, Qi LM (2008) Chem Mater 20:3965–3972
47. Baker H (1992) ASM handbook, vol 3. Alloy Phase Diagram, ASM International, Materials Park
48. Wang YW, Zhang LD, Meng GW, Peng XS, Jin YX, Zhang J (2002) J Phys Chem B 106:2502–2507